*Article*

# Dual-Modality Imaging Microfluidic Cytometer for Onsite Detection of Phytoplankton

**Bo Xiong [1], Tianqi Hong [1], Herbert Schellhorn [2] and Qiyin Fang [1,3,*]**

[1] School of Biomedical Engineering, McMaster University, 1712 Main St W, Hamilton, ON L8S 4L8, Canada; xiongb3@mcmaster.ca (B.X.); hongt6@mcmaster.ca (T.H.)

[2] Department of Biology, McMaster University, 1712 Main St W, Hamilton, ON L8S 4L8, Canada; schell@mcmaster.ca

[3] Department of Engineering Physics, McMaster University, 1712 Main St W, Hamilton, ON L8S 4L8, Canada

[*] Correspondence: qiyin.fang@mcmaster.ca

**Abstract:** Phytoplankton monitoring is essential for better understanding and mitigation of phytoplankton bloom formation. We present a microfluidic cytometer with two imaging modalities for onsite detection and identification of phytoplankton: a lensless imaging mode for morphological features, and a fluorescence imaging mode for autofluorescence signal of phytoplankton. Both imaging modes are integrated in a microfluidic device with a field of view (FoV) of 3.7 mm × 2.4 mm and a depth of field (DoF) of 0.8 mm. The particles in the water flow channel can be detected and classified with automated image processing algorithms and machine learning models using their morphology and fluorescence features. The performance of the device was demonstrated by measuring *Chlamydomonas*, *Euglena*, and non-fluorescent beads in both separate and mixed flow samples. The recall rates for *Chlamydomonas* and *Euglena* ware 93.6% and 94.4%. The dual-modality imaging approach enabled observing both morphology and fluorescence features with a large DoF and FoV which contribute to high-throughput analysis. Moreover, this imaging flow cytometer platform is portable, low-cost, and shows potential in the onsite phytoplankton monitoring.

**Keywords:** flow cytometry; phytoplankton; lensless imaging; fluorescence imaging; miniaturization; microfluidic

## 1. Introduction

Phytoplankton play a vital role in the aquatic ecosystem [1,2]. However, species composition, concentration, and distribution of phytoplankton change frequently while the drivers of these changes are not fully understood [3]. Phytoplankton bloom, a rapid growth in the algal population, can readily occur under favorable environmental conditions, posting a threat to human and ecosystem health, and resulting in economic losses in agriculture [4]. For example, some phytoplankton species produce toxins are harmful to both fish and humans [5]; algae bloom can result in oxygen depletion, killing fish and benthic organisms [6]. Therefore, it is necessary to closely monitor the phytoplankton bloom development for better mitigation strategies [7–9]. Conventional phytoplankton detection relies on its autofluorescence signatures and morphological features. Currently, both methods are performed by laboratory instruments (e.g., fluorometers and microscopes) and require manual sampling handling [10–12]. Such approach is time-consuming and expensive due to the needs of manual steps by experienced technical staff. Thus, there is a pressing need for low-cost and efficient identification techniques that can detect the species composition and concentration of phytoplankton in situ.

Several commercial instruments based on fluorescent spectroscopic sensing are available for onsite phytoplankton monitoring where concentration of chlorophyll and other pigments (such as phycocyanin, phycoerythrin, and carotenoids) can be estimated based on their autofluorescence [13,14]. With these instruments, the phytoplankton can be classified

into a few major groups based on their color, such as green algae, red algae, and blue-green algae. That said, the fluorometers cannot count phytoplankton cells/colonies and further classification of phytoplankton species is difficult when multiple species of phytoplankton are presented in the water sample [15].

Imaging-based flow cytometry, which combines microscopy and flow cytometry, is a powerful technology that can be used for observation and identification of phytoplankton at the cellular level [16–19]. A sheath flow is used to confine the sample particles to a focus point of a microscope objective lens. Then, morphology features and autofluorescence can be measured for particle classification. To capture images with micrometer-level resolution, microscope objectives with high numerical aperture are used. As a result, the field of view (FoV) and depth of focus (DoF) are reduced, leading to limited volumetric throughput and the need for focus adjustments [20]. At present, the imaging-based flow cytometers are typically bulky and expensive [20–22], limiting their use in onsite monitoring.

Lensless imaging provides an alternative microscopic approach, in which the shadow of a sample is recorded on an image sensor directly [23,24]. Lensless imaging has several advantages over conventional microscopes including large FoV, large DoF simple alignment, cost-effectiveness, and portability. When a coherent light source is used, the shadows with fringe interference patterns can be observed. Then, the samples in a wide range of depths can be observed with high-spatial resolution after holographic reconstruction [25,26]. Recently, lensless imaging has been used for morphological observation of particles/cells in the fluidic samples, such as characterization of microplastics [27], urine analysis [28,29], blood analysis [30], and phytoplankton analysis [31]. Nevertheless, a separate fluorescence analysis measurement is still commonly required in phytoplankton identification [12,17,21,22,32].

A fluorescence lensless setup has been reported by inserting an emission filter between image sensor and fluidic channel [23]. However, the resolution of lensless fluorescence imaging is limited by the point spread function (PSF), which is dominated by the distance between particles/cells and image sensor [23]. Considering a typical distance of 200 μm, the imaging resolution is about 200 μm [23,33,34], which is insufficient for phytoplankton analysis. Recently, several techniques have been investigated to improve the resolution of fluorescence lensless imaging including hardware designs and computational algorithms [23]. The spatial resolution can be improved by digital deconvolution of incoherent PSF which require precise distance between the detected cell and imager [33]. However, this distance is unknow when a cell is flowing flow through a fluidic channel without hydrodynamic focusing. Custom-fabricated imagers with nanostructures/microstructures designs have been investigated to improve the resolution of fluorescence lensless imaging [35]. Higher resolution can be realized when the samples are closed to the nanostructures/microstructures or placed at particular regions in the device. These methods also reduce DoF and/or FoV dramatically [36] and require expensive custom-fabricated imagers, limiting their use in onsite phytoplankton monitoring.

In this work, we developed a dual-modality imaging microfluidic cytometry approach where a lensless imaging mode is integrated with a fluorescence mode with a lens. This dual-modality imaging approach enables large FoV and DoF, while keeping device cost low and portable for onsite detection and identification of phytoplankton. This technique allows single-cell analysis without using bulky and expensive microscope setups. In the lensless imaging mode, shadow and fringe patterns of each particle are captured by a lensless camera. In the fluorescence imaging mode, autofluorescence is measured by another camera with an excitation light and an emission filter. Image processing algorithms and machine learning models have been developed to facilitate automated phytoplankton detection and classification in the water samples with integrated morphology and fluorescence features. To evaluate the feasibility of the design experimentally, two phytoplankton species commonly found in surface water sources *Chlamydomonas* and *Euglena* were chosen since their sizes are within in the typical size range (from 1–1000 μm) of phytoplankton [37]. The two species are also widely distributed, easy to be cultured as

standard reference samples [38,39], and have been tested in environmental applications with the use of wastewater effluent as a nutrient medium [40]. The performance of the device was evaluated by measuring *Chlamydomonas*, *Euglena*, and 10 μm non-fluorescent beads in both separate and mixed flow samples.

## 2. Materials and Methods

### 2.1. Materials

Phytoplankton samples: *Chlamydomonas* (CPCC 243) and *Euglena* (CPCC 95), were purchased from Canadian Phycological Culture Centre (Waterloo, ON, Canada). *Chlamydomonas* and *Euglena* contain Chlorophyll a, which emits fluorescent light with a peak of 690 nm under blue or ultraviolet excitation (400–450 nm) [41]. For comparison purposes, 10 μm polystyrene (PS) beads (Polysciences, Warrington, PA, UK) are used. Excitation and illumination diode lasers at 405 nm and 632 nm were used (Wuhan Besram Technology, Wuhan, China). Low-cost cameras (Raspberry Pi camera v2, Raspberry Pi Foundation, Cambridge, UK) were used to build customized camera modules. Customized glass slides with a thickness of 0.33mm (Luoyang Ancient Glass Ltd. Co., Luoyang, China) and Polydimethylsiloxane (PDMS) (Sylgard 184, Dow Corning, Midland, MI, USA) were used to build the microfluidics channels.

### 2.2. System Design

A schematic of the microfluidic imaging flow cytometer with two cameras is shown in Figure 1a. The imaging lens was removed from a camera for lensless imaging. A microfluidic chip was placed above the image sensor. The FoV of the lenless camera is 3.7 mm × 2.4 mm which is equal to the dimension of the image sensor. In the lensless imaging mode, a 632 nm laser is used for illumination. Thus, the particles' shadows and the interference pattens can be recorded on the image sensor. In the fluorescence imaging mode, a 405 nm laser is used for excitation. Another camera with a built-in lens was placed 2.5 cm above the microfluidic chip to acquire the fluorescence images. The built-in lens position was adjusted to allow focusing on the fluidic channel. A long-pass emission filter (WRATTEN No. 29, λ > 590 nm, Eastman Kodak, Rochester, NY, USA) was mounted in front of the lens of fluorescence camera to reject the 405 nm excitation light. The two lasers were modulated synchronously with their respective cameras such that each imaging mode operates at different time cycles to avoid interference, i.e., the red fluorescence images can be captured in the fluorescence imaging mode when the 405 nm laser is switched on while the 632 nm laser is switched off. Similarly, the lensless images at 632 nm are acquired when the 405 nm laser is switched off.

The optical module is housed by a custom-made compact (20 cm × 15 cm × 15 cm) enclosure with 3D printed mounts for each component (e.g., lasers, cameras, and microfluidic chips. The output of the laser diodes has an approximate 5 mm diameter circular profile on the sample without additional optics.

A block diagram of the experimental setup is shown in Figure 1b. A microcontroller (Uno, Arduino, Somerville, MA, USA) sent two synchronized 1.8 Hz square waves to two lasers. Since the phase difference between two square waves was 180°, the illuminations from two lasers are separated in time. Fluid samples were delivered into the microfluidic channel with a flow rate of 3 mL/h (0.83 μL/s) using a syringe pump. Two microcomputers (Raspberry pi 4) were used to control two cameras and record videos at 25 frames per second (fps). The exposure time of the fluorescence mode was 15 ms/frame and the holographic mode was 2 ms/frame, respectively. The two microcomputers are interfaced together to the controller to maintain the synchronization between the cameras and lasers. A few frames are shown in Figure 2 to illustrate the acquired lensless images and fluorescence images. The recorded videos were processed off-line on a separate computer workstation. The total cost of the main modules, including sensing unit, microcomputers, microcontroller, and lasers, is less than USD 300 (not including the computer workstation for image processing).
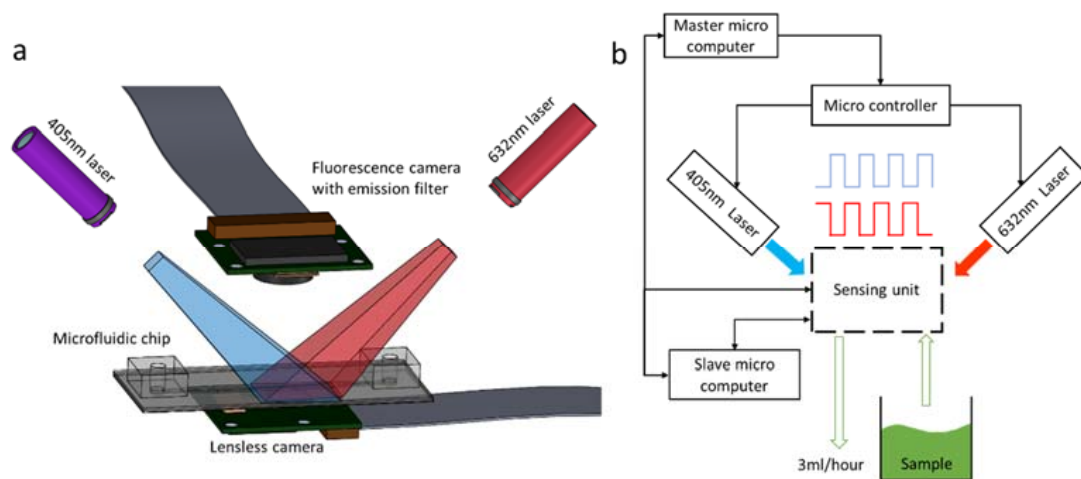
**Figure 1.** (**a**) The schematic of imaging microfluidic flow cytometer, including a microfluidic chip, a lensless camera, a fluorescence camera and two lasers. A fluidic channel is illuminated by a 405 nm laser and a 632 nm laser alternatively in time. The lensless camera is placed beneath a microfluidic chip and matches the illumination area. The fluorescence camera is placed above the microfluidic chip. A 590 nm log-pass filter is mounted on the camera lens to block the 405 nm excitation light for fluorescence imaging. (**b**) The block diagram of experimental setup. The sensing unit in the block diagram includes two cameras and a microfluidic chip.
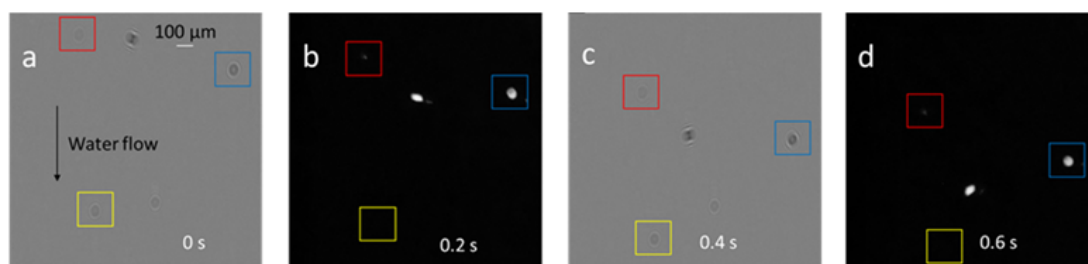


**Figure 2.** Four frames (**a**–**d**) captured at 0 s, 0.2 s, 0.4 s, and 0.6 s, respectively (see Supplementary Video S1). (**a**,**c**) are captured in the lensless imaging mode. (**b**,**d**) are captured in the fluorescence imaging mode. The direction of water flow and 100 µm scale bar is shown in (**a**). A *Chlamydomonas* cell (red), a *Euglena* cell (blue), and a 10 µm PS bead (yellow) are labeled in these four frames.

### 2.3. Microfluidic Chip Design

The microfluidic chip design features a removable flow module separate from the lensless camera. As shown in Figure 3a, the removable flow module consisted of three glass slides: a top layer, a middle layer, and a bottom layer. The height of the fluidic channel was 0.33 mm, which depends on the thickness of middle layer. The width of water channel was 2.6 mm, covering an active area of 6.2 mm$^2$ (2.6 mm × 2.4 mm) on the image sensor. A PDMS adaptor was bonded to the top layer for tubes insertion. The removable flow module was mounted on the lensless camera using a 3D printed adaptor. The distance between the fluidic channel and the image sensor was about 1 mm. After each use, the removable flow module can be replaced while the rest of the device does not need to be disposed. The flow chips can also be reused after cleaned by detergent to minimize cost and waste.
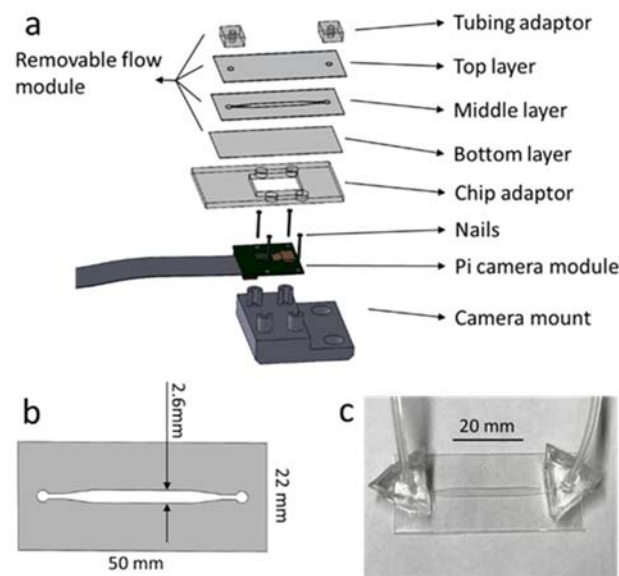
**Figure 3.** Description of chip design. (**a**) A explode view of the microfluidic chip and the lensless camera. (**b**) A top view of the middle layer which determine the shape and thickness of the fluidic channel. (**c**) A photo of the removable flow module.

### 2.4. Image Processing Algorithms

Detection and tracking algorithms were developed in Python with OpenCV and Sklearn, as shown in Figure 4. The background is subtracted to remove the particles adhering to the microfluidic channel walls in the videos. Histogram of oriented gradients (HOG) and support vector machine (SVM) were used to detect particles in the lensless imaging mode [42]. Once a particle was detected, a discriminative correlation filter with channel and spatial reliability (CSR-DCF) was used to track particles between frames [43]. Alternatively, particles could be tracked with Kalman filter when the fluorescence imaging mode was on or the CSR-DCF tracker failed. The view of the fluorescence camera was aligned with the view of lensless camera by co-registration of the two imaging modes without the sample. Hence, particles can be tracked between both imaging modes.
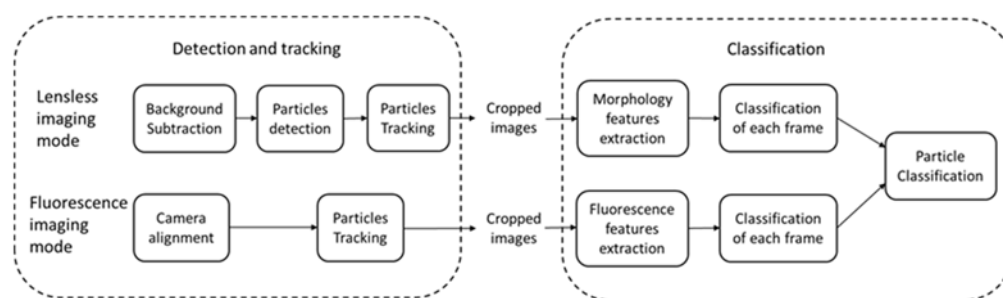


**Figure 4.** The logic flow of image processing algorithms. Particles are detected and tracked in the consecutive frames and both cropped lensless images and cropped fluorescence images are obtained. Then, particles can be classified with integrated morphology features and fluorescence features.

Particle classifications make use of a combination of fluorescence and morphology features. In the lensless imaging mode, the particles' morphology features were extracted using HOG descriptor from their corresponding cropped images. Here, raw holograms without holographic reconstruction were used for morphology analysis to reduce computation workload. In the fluorescence imaging mode, the particles' fluorescent features including total pixel value, averaged pixel value, dimension, and peak pixel value were calculated form their corresponding region of interest (ROI). Then, two SVM classifiers

were trained for lensless imaging mode and fluorescence imaging mode, respectively. As a particle was detected and tracked in the consecutive frames, classification was performed once per frame using the two SVM classifiers and the final particle classification is calculated from the equally weighted sum of the two classifiers.

### 2.5. Sample Preparation

In order to obtain the ground truth for classifier training and testing, three samples were prepared by diluting *Chlamydomonas*, *Euglena*, and PS beads samples in Bold's Basal Medium (BBM), respectively. To evaluate the system performance, six more samples were prepared. Three samples were prepared by diluting a *Chlamydomonas* sample using different dilution ratios. The other three samples were prepared by mixing *Chlamydomonas*, *Euglena*, PS beads samples, and BBM. Their compositions are shown in Table 1. We found that unintended contaminations were presented in both *Chlamydomonas* and *Euglena* samples. Since these particles are not fluorescent, they can be distinguished from phytoplankton cells clearly with fluorescence images.

**Table 1.** Composition of samples.

| Sample ID | *Chlamydomonas* | *Euglena* | PS Beads | BBM | Total |
|---|---|---|---|---|---|
| # 1 | 0 mL | 0 mL | 1 mL | 29 mL | 30 mL |
| # 2 | 0 mL | 2 mL | 0 mL | 28 mL | 30 mL |
| # 3 | 1.5 mL | 0 mL | 0 mL | 28.5 mL | 30 mL |
| # 4 | 0.5 mL | 0 mL | 0 mL | 29.5 mL | 30 mL |
| # 5 | 1 mL | 0 mL | 0 mL | 29 mL | 30 mL |
| # 6 | 2 mL | 0 mL | 0 mL | 28 mL | 30 mL |
| # 7 | 0.33 mL | 0.67 mL | 0 mL | 29 mL | 30 mL |
| # 8 | 0.33 mL | 1.33 mL | 0 mL | 28.33 mL | 30 mL |
| # 9 | 0.33 mL | 0.67 mL | 0.4 mL | 28.67 mL | 30 mL |

## 3. Results

### 3.1. Particle Classification

The particle classification algorithms were trained and tested using *Chlamydomonas*, *Euglena*, and PS beads samples (samples #3, #2, and #1). A dataset was generated for SVM classifier training and testing, as shown in Figure 5. The dataset contains 1152 fluorescent particles found in the *Chlamydomonas* sample, 1049 fluorescent particles found in the *Euglena* sample, and 1350 non-fluorescent particles found in the PS beads sample. The non-fluorescent contamination found in the *Chlamydomonas* and *Euglena* samples was excluded. These particles are linked to 73,068 cropped lensless images and 72,444 cropped fluorescent images obtained from the videos using the detection and tracking algorithms.

An example of captured fluorescence images of a 10 μm polystyrene bead, a *Chlamydomonas* cell and a *Euglena* cell are shown in Figure 6a–c. The corresponding cropped images captured in the lensless imaging mode are shown in Figure 6d–f. For better visualization of cropped images captured in the lensless imaging mode, holographic reconstruction was performed with angular spectrum method [44]. These reconstructed images are shown in Figure 6g–i. The samples were observed with a benchtop microscope, and the typical images of *Chlamydomonas*, *Euglena*, and PS beads under a microscope were shown in Figure 6j–l. Since *Chlamydomonas* and *Euglena* contain Chlorophyll a, they can be seen in the fluorescence imaging mode. On the other hand, PS beads are hardly observed in the fluorescence imaging mode as they are not fluorescent. A *Euglena* cell is typically larger than *Chlamydomonas*. As a result, *Euglena* cells emit stronger fluorescence, and their shadow and optical fringes are clearer. *Chlamydomonas* cells and PS beads have similar size and shape, as shown in Figure 6. As a result, it is difficult to distinguish them only using morphology features in the lensless imaging mode.
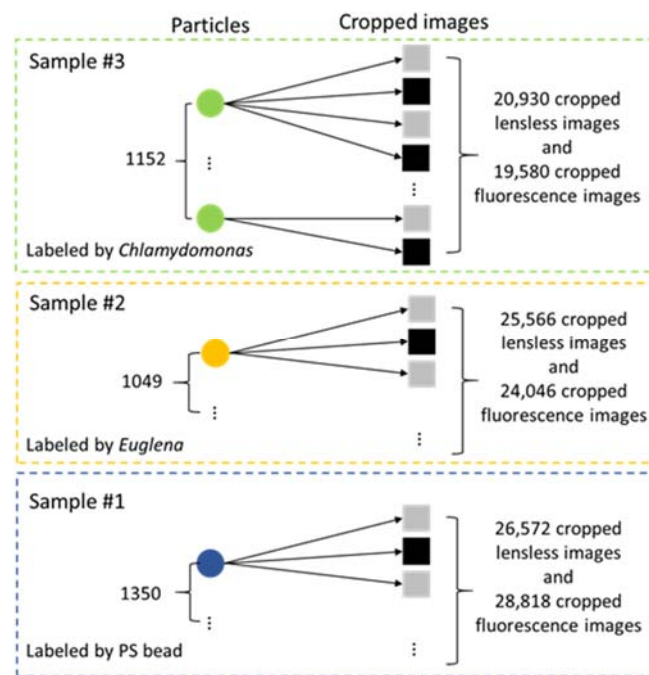
**Figure 5.** Overview of a particle dataset. In total, there are 3551 particles and their corresponding *Chlamydomonas* 145,512 cropped images in the dataset. These particles and cropped images are labelled by *Chlamydomonas*, *Euglena*, and PS bead.
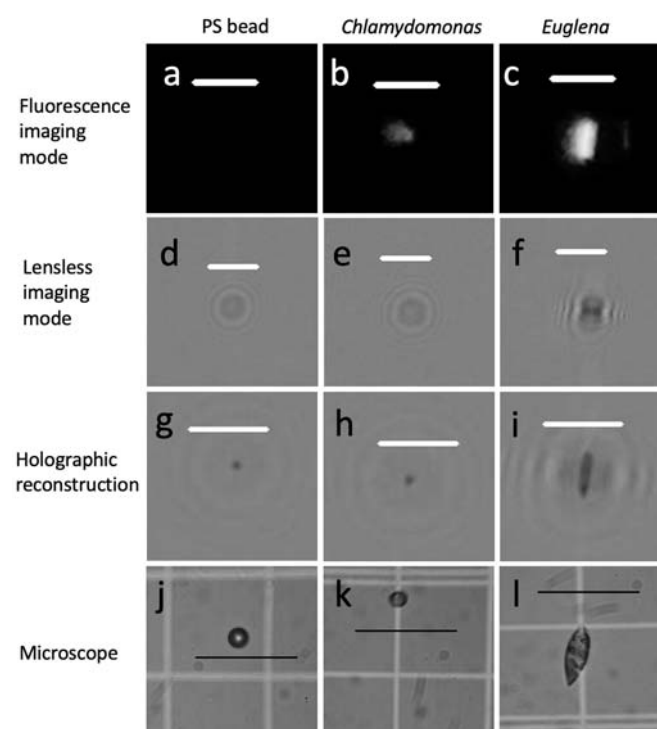


**Figure 6.** Images of 10 μm polystyrene bead, *Chlamydomonas* cell, and *Euglena*. (**a**–**c**) are captured in the fluorescence imaging mode. (**d**–**f**) are captured in the lensless imaging mode. For better visualization, holographic reconstructed images are shown in (**g**–**i**). Samples were observed a microscope with a magnification of 400. Their typical images are shown in (**j**–**l**). Scale bars are 100 μm.

The dataset was split into a training set and a testing set with a 50–50 ratio. Then, two SVM classifiers were trained using the training set. The morphology features were

extracted from the cropped lensless images to train the first SVM classifier; the fluorescence features were extracted from the cropped fluorescence images to train the second SVM classifier. The particles in the testing set were classified by integrating two SVM classifiers, and the results of particle classification are shown in Table 2. For comparison purposes, the particles were also classified with individual classifiers, and the results are shown in Tables 3 and 4. When both SVM classifiers and dual-modality imaging are used, the classification performance is the best among three groups of samples. The recall rates of *Chlamydomonas*, *Euglena*, and 10 μm PS beads are 0.936, 0.944, and 1.000, respectively. These results demonstrate the efficiency of particles classification in the dual-modality imaging approach. There are some low fluorescence objects in the sample. They are likely the dead cells due to shipping and sample preparation.

**Table 2.** Confusion matrix of classifier using lensless images and fluorescent images.

| Class | Predicted: *Chlamydomonas* | Predicted: *Euglena* | Predicted: PS Bead |
|---|---|---|---|
| Actual: *Chlamydomonas* | 0.936 | 0.005 | 0.059 |
| Actual: *Euglena* | 0.016 | 0.944 | 0.041 |
| Actual: PS bead | 0.000 | 0.000 | 1.000 |

**Table 3.** Confusion matrix of classifier using fluorescent images. PS beads cannot be detected in the fluorescence imaging mode since their fluorescence is too weak.

| Class | Predicted: *Chlamydomonas* | Predicted: *Euglena* | Predicted: PS Bead |
|---|---|---|---|
| Actual: *Chlamydomonas* | 0.831 | 0.005 | 0.163 |
| Actual: *Euglena* | 0.016 | 0.897 | 0.087 |
| Actual: PS bead | \ | \ | \ |

**Table 4.** Confusion matrix of classifier using lensless images.

| Class | Predicted: *Chlamydomonas* | Predicted: *Euglena* | Predicted: PS Bead |
|---|---|---|---|
| Actual: *Chlamydomonas* | 0.817 | 0.028 | 0.155 |
| Actual: *Euglena* | 0.043 | 0.924 | 0.033 |
| Actual: PS bead | 0.040 | 0.022 | 0.937 |

### 3.2. Particle Counting

The imaging flow cytometer was tested with four *Chlamydomonas* samples with different dilution ratios (Sample #3 to Sample #6). Figure 7 shows the automated counting results response to the *Chlamydomonas* concentration. The dotted line shows a result of linear fitting with a correlation coefficient of 0.9835. These results demonstrate the performance of automate particles counting with detection and tracking algorithms. The obtained error bars were larger than the theoretical detection limits since the imaging flow cytometer should be able to detect single particle in the samples. There are two explanations to the large error bars: (i) the actual cell counts in every 150 uL samples could be different; (ii) the detection and tracking algorithms are not optimized.
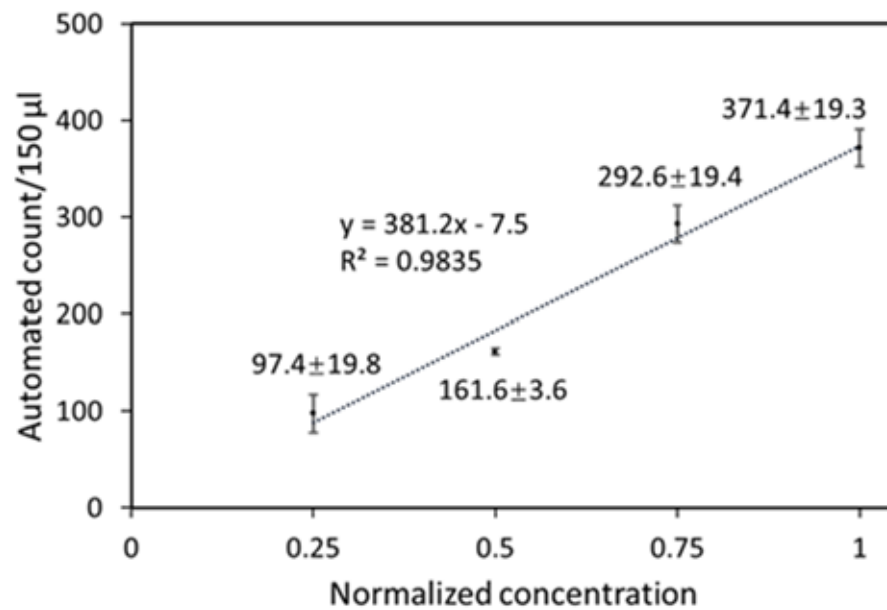
**Figure 7.** The *Chlamydomonas* count per 150 uL in the four samples. The ratio of *Chlamydomonas* concentration among samples #4, #5, #3, and #6 are 1:2:3:4. The error bar is estimated using standard deviation (SD) among 5 trials at each point. Each trial took 3 min as 150 uL water sample flows through the water channel.

The imaging flow cytometer was tested with three mixed samples to demonstrate its efficiency in detecting and counting specific cells. Sample #7 contained *Chlamydomonas* and *Euglena*. The concentration of *Euglena* in sample #8 was doubled compared with that in sample #7. In sample #9, the concentration of *Chlamydomonas* and *Euglena* were same with that in sample #7, while additional PS beads were added. The automated counting results of these mixed samples are shown and compared in Figure 8. A baseline is measured with Sample #7 for comparison purposes. Note that detected non-fluorescent particles are the contamination in sample #7. Figure 8a shows that the doubling of *Euglena* concentration (182.6 ± 24.9 vs. 106.7 ± 11.2) was correctly detected and counted. Figure 8b shows that both *Chlamydomonas* concentration (52.1 ± 9.2 vs. 63.4 ± 13.5) and *Euglena* concentration (111.7 ± 15.0 vs. 106.7 ± 11.2) are correctly detected and counted when additional PS beads were presented. It also shows that non-fluorescent PS beads were detected and counted. These results demonstrate that the dual modality system can detect and count phytoplankton cells (*Chlamydomonas* and *Euglena*) when these two species and non-fluorescent particles are mixed in a sample.
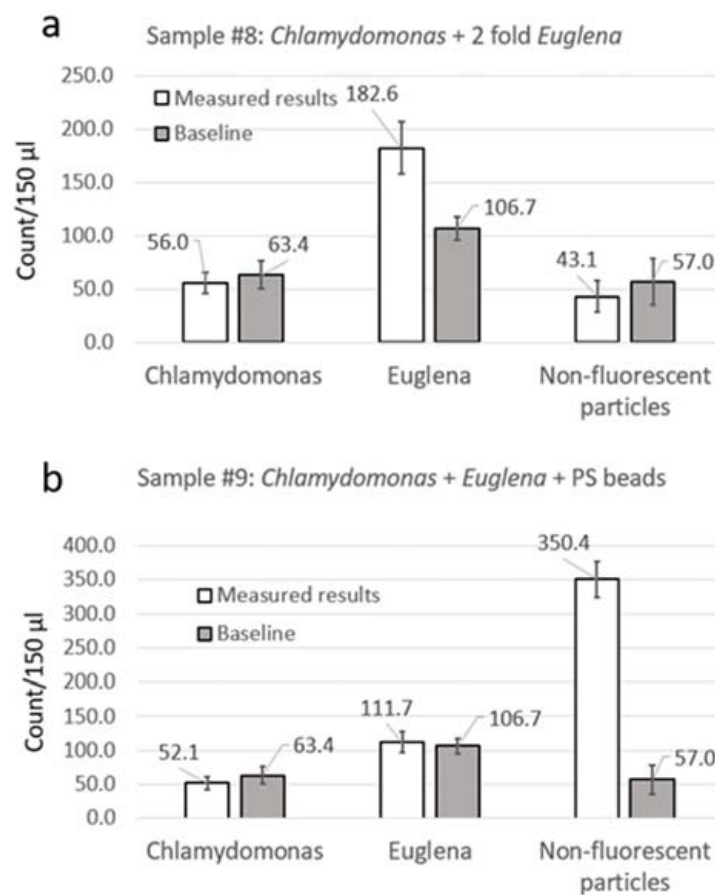
**Figure 8.** The measurement results of mix samples. Baseline is measured with Sample #7 for comparison purposes. Measured results of sample #8 and sample #9 were shown in (**a**,**b**), respectively. The error bar is estimated using standard deviation (SD) among 5 trails at each point. Each trail takes 3 min as 150 uL water sample flow through the water channel.

## 4. Discussion

In this manuscript, we report a dual-modality imager that is capable of low cost, onsite detection, and identification of some phytoplankton species in water. The feasibility and the performance of the design are validated experimentally using two typical waterborne phytoplankton species: *Chlamydomonas* and *Euglena* as examples. Our results demonstrated that the integration of morphological features from lensless holographic mode and functional features from autofluorescence signals are effective and can significantly improve classification. Even with a small image sensor, the FoV and DoF are large in this design and can lead to significant improvement in throughput under the same conditions.

In real-world algae detection and diagnosis, there exists multiple phytoplankton targets of interest (e.g., *Chlamydomonas, Euglena, diatoms*) [38–40,45]. Our dual modality approach added autofluorescence as an additional source of contrast to morphological features from holographic shadow imaging; we have demonstrated that it can be used to differentiate the two species. In future studies, we plan to expand on this technique to additional phytoplankton species. For example, larger FoV detectors with multiple flow channels coupled with multiplexed fluorescence emission filters for targets with different autofluorescence emission characteristics, and/or using fluorescence lifetime with frequency domain imaging [46]. Among these potential approaches, 400–450 nm is sufficient to excite most phytoplankton species while a multiple spectral sensor device with monolithically integrated bandpass filters [47]. As a result, the footprint, complexity, and cost of the device can remain low.

### 4.1. Performance of Fluorescence Mode

The fluorescence of chlorophyll a can be excited over a broad spectral band in the visible with emission in the far red (630–700 nm). Excitation at 405 nm was chosen as it is sufficient to excite chlorophyll and far from the emission band, which allows the use of a low-cost long pass filter. The fluorescence imaging mode relayed on a compact camera with a built-in lens and a fixed aperture of f/2.8. Although its spatial resolution does not measure up with that of benchtop microscopes, it has a long DoF and a capability of detecting *Chlamydomonas* cells. To demonstrate this, a few *Chlamydomonas* cells were imaged multiple times as the height offset of image plane was varied from −1 mm to 0.6 mm. *Chlamydomonas* cells can be detected using fluorescence camera even if these cells are out-of-focus, as shown in Figure 9b,c,e. However, their morphology features are hard to obtain because the observed *Chlamydomonas* cells are blurred and have varied sizes in response to height offset. The radius of observed *Chlamydomonas* cells was calculated and shown in Figure 9a. These results indicate that the fluorescence camera can detect the fluorescence signals generated by *Chlamydomonas* cells with a DoF of more than 0.8 mm. The large DoF can provide two advantages: (i) higher volumetric throughput since thick fluid channel can be applied (ii) better resistance to the unintended focus change. Since the morphology features can be obtained in the lensless imaging mode, the identification of particles is less affected by the poor spatial resolution of fluorescence camera.
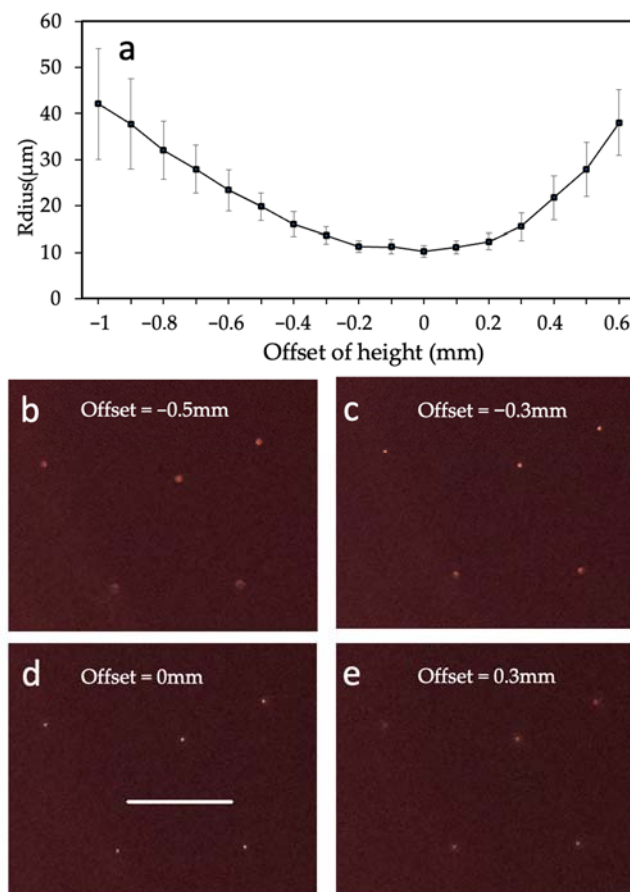


**Figure 9.** (**a**) The radius of observed *Chlamydomonas* cells in response to the offset of image plane. The plane with 0 offset is determined by the focus plane where radius of observed *Chlamydomonas* cells is minimum. The radius is defined as the distance between the peak value and 10% value. (**b–e**) shows the fluorescence images captured at offsets of −0.5 mm, −0.3 mm, 0 mm, 0.3 mm, respectively. The scale bar is 500 μm.

### 4.2. Volumetric Throughput

The volumetric throughput of this imaging flow cytometer platform is determined by several factors, including FoV, DoF, camera frame rate, and sensitivity of image sensor (ISO). Compared with traditional microscopes, the proposed dual-modality imaging approach offers advantages of large FoV and large DoF, even with a small camera. Besides the optical design, the system can be integrated with a concentration mechanism to preprocess the sample, which increases the concentration by 500–1000 fold [48]. Additionally, the volumetric throughput of current platform is limited by the low-cost cameras with small active sensing area and sensitivity. A significant benefit of microfluidic sensing systems is the feasibility of multiplexing with multiple channels to increase throughput. The frame rate of the Pi camera is low, leading to errors in particles tracking and counting when flow rate is high. Moreover, the sensitivity of the image sensor is low. Therefore, fluorescence imaging requires a long exposure time (~15 ms), resulting in motion blurring when particles move fast. The throughput can also be improved by using cameras with high ISO and larger active sensing area. Since the camera technologies are evolving rapidly, mostly benefiting from the mobile device market, these limitations of low-cost cameras could be overcome in the future.

In the holographic lensless imaging mode, the FoV and DoF are optimized using the lensless imaging model in order to improve throughput. Many holographic imaging-based devices will require image reconstruction, which is typically the bottleneck for system throughput. The reconstructed imaging features are useful for human to evaluate and select for classification. In our system, a machine learning algorithm for classification with different features (morphological and functional). As a result, the morphological features used in classification are already contained in the holographic images without the need for reconstruction. This approach significantly reduced the computation requirement of the system design, which will lead to reduction in cost and computation time.

### 4.3. Analysis of Natural Water

Natural water samples were manually collected from Lake Ontario (Bayfront Park, Hamilton, ON, Canada), followed by observation using the dual-modality imaging system. Some suspended particles that could be phytoplankton cells or colonies were detected by the dual-modality imaging system. Figure 10 shows three particles found in the natural water samples. Their fluorescence features can be observed in the fluorescence mode. Their morphology features can be observed in the raw images captured in the lensless mode as well as the holographic reconstructed images. Classifiers that take advantages of morphology and fluorescence features can be trained for phytoplankton identification of natural water samples in the future. The video encoder on the Raspberry Pi deteriorated interference patterns in the raw holograms, reducing the quality of reconstructed images. Thus, the presented imaging processing algorithms still use morphology features extracted from raw holograms by HOG. Advance hardware and algorithms could be used to assist holographic reconstruction, improving morphology analysis in the future.
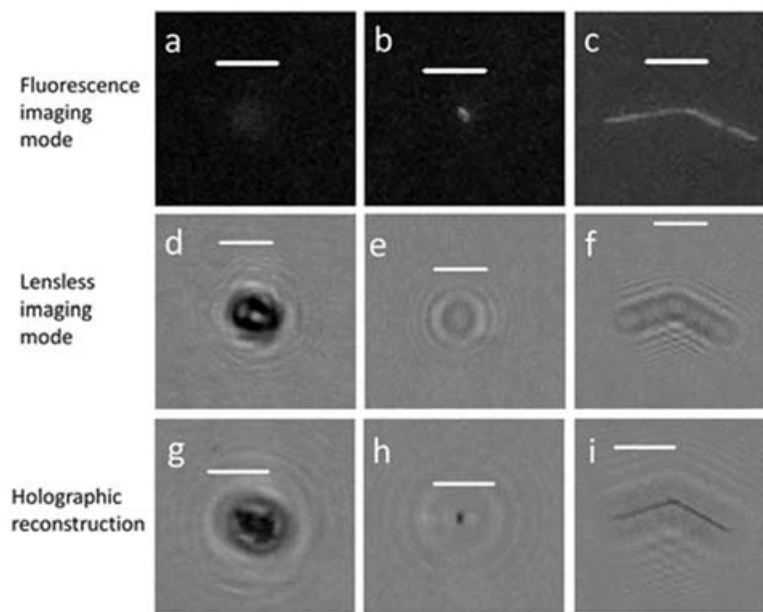
**Figure 10.** Images captured using natural water samples: the fluorescence mode (**a**–**c**), the lensless mode (**d**–**f**). (**g**–**i**) are holographic reconstruction results of (**d**–**f**). Scale bar is 100 μm.

## 5. Conclusions

We present a dual-modality imaging microfluidic cytometer for onsite phytoplankton monitoring. The combination of a coherent lensless imaging mode and a fluorescence imaging mode with lens allows high throughput detection with large FoV and DoF in a thick fluidic channel (0.33 mm). With a machine learning approach, co-registered morphological (lensless) and autofluorescence (fluorescence) features from the two imaging modes are used to achieve accurate and sensitive detection. Experiments with *Chlamydomonas*, *Euglena*, 10 μm PS beads, and mixed samples have been performed to demonstrate the efficiency of particle counting and single-cell classification. The cost-effectiveness and compactness of this design make it promising approach for onsite water monitoring.

**Conflicts of Interest:** The authors declare no conflict of interests.

## References

1. Field, C.B.; Behrenfeld, M.J.; Randerson, J.T.; Falkowski, P. Primary production of the biosphere: Integrating terrestrial and oceanic components. *Science* **1998**, *281*, 237–240. [CrossRef]
2. Carpenter, S.R.; Kitchell, J.F.; Hodgson, J.R.; Cochran, P.A.; Elser, J.J. Regulation of lake primary productivity by food web structure. *Ecology* **1987**, *68*, 1863–1876. [CrossRef]
3. Benincà, E.; Huisman, J.; Heerkloss, R.; Jöhnk, K.; Branco, P. Chaos in a long-term experiment with a plankton community. *Nature* **2008**, *451*, 822–825. [CrossRef]
4. Sahoo, D.; Seckbach, J. *The Algae World*; Springer: Dordrecht, The Netherlands, 2015.
5. Grattan, L.M.; Holobaugh, S.; Morris, K.G., Jr. Harmful algal blooms and public health. *Harmful Algae* **2016**, *57*, 2–8. [CrossRef]
6. Hallegraeff, G.M. A review of harmful algal blooms and their apparent global increase. *Phycologia* **1993**, *32*, 79–99. [CrossRef]
7. Gallardo-Rodríguez, J.J.; Astuya-Villalón, A.; Llanos-Rivera, A.; Avello-Fontalba, V.; Ulloa-Jofré, V. A critical review on control methods for harmful algal blooms. *Rev. Aquacult.* **2019**, *11*, 661–684. [CrossRef]
8. Martin, J.L.; Hanke, A.R.; LeGresley, M.M. Long term phytoplankton monitoring, including harmful algal blooms, in the Bay of Fundy, eastern Canada. *J. Sea Res.* **2009**, *61*, 76–83. [CrossRef]
9. Lee, J.H.W.; Hodgkiss, I.J.; Wong, K.T.M.; Lam, I.H.Y. Real time observations of coastal algal blooms by an early warning system. *Estuar. Coast. Shelf Sci.* **2005**, *65*, 172–190. [CrossRef]
10. Lomax, A.S.; Corso, W.; Etro, J.F. Employing unmanned aerial vehicles (UAVs) as an element of the Integrated Ocean Observing System. In Proceedings of the OCEANS 2005 MTS/IEEE, Washington, DC, USA, 17–23 September 2005; pp. 184–190.
11. Coltelli, P.; Barsanti, L.; Evangelista, V.; Frassanito, A.M.; Gualtieri, P. Water monitoring: Automated and real time identification and classification of algae using digital microscopy. *Environ. Sci.* **2014**, *16*, 2656–2665. [CrossRef] [PubMed]
12. Wilde, E.W.; Fliermans, C.B. Fluorescence microscopy for algal studies. *Trans. Am. Microsc. Soc.* **1979**, *98*, 96–102. [CrossRef]
13. Beutler, M.; Wiltshire, K.H.; Meyer, B.; Moldaenke, C.; Lüring, C. A fluorometric method for the differentiation of algal populations in vivo and in situ. *Photosynth. Res.* **2002**, *72*, 39–53. [CrossRef]
14. Izydorczyk, K.; Carpentier, C.; Mrówczyński, J.; Wagenvoort, A.; Jurczak, T.; Tarczyńska, M. Establishment of an Alert Level Framework for cyanobacteria in drinking water resources by using the Algae Online Analyser for monitoring cyanobacterial chlorophyll a. *Water Res.* **2009**, *43*, 989–996. [CrossRef]
15. Shin, Y.H.; Barnett, J.Z.; Gutierrez-Wing, M.T.; Rusch, K.A.; Choi, J.W. A hand-held fluorescent sensor platform for selectively estimating green algae and cyanobacteria biomass. *Sens. Actuators B Chem.* **2018**, *262*, 938–946. [CrossRef]
16. Wert, E.C.; Dong, M.M.; Rosario-Ortiz, F.L. Using digital flow cytometry to assess the degradation of three cyanobacteria species after oxidation processes. *Water Res.* **2013**, *47*, 3752–3761. [CrossRef] [PubMed]
17. Wu, J.; Li, J.; Chan, R.K.Y. A light sheet based high throughput 3D-imaging flow cytometer for phytoplankton analysis. *Opt. Express* **2013**, *21*, 14474–14480. [CrossRef]
18. Park, J.; Kim, Y.; Kim, M.; Lee, W.H. A novel method for cell counting of Microcystis colonies in water resources using a digital imaging flow cytometer and microscope. *Environ. Eng. Res.* **2019**, *24*, 397–403. [CrossRef]
19. Rutten, T.P.A.; Sandee, B.; Hofman, A.R.T. Phytoplankton monitoring by high performance flow cytometry: A successful approach? *Cytom. Part A J. Int. Soc. Anal. Cytol.* **2005**, *64*, 16–26. [CrossRef]
20. Han, Y.; Gu, Y.; Zhang, A.C.; Lo, Y.H. Imaging technologies for flow cytometry. *Lab Chip* **2016**, *16*, 4639–4647. [CrossRef] [PubMed]
21. Dashkova, V.; Malashenkov, D.; Poulton, N.; Vorobjev, I.; Barteneva, N.S. Imaging flow cytometry for phytoplankton analysis. *Methods* **2017**, *112*, 188–200. [CrossRef]
22. Olson, R.J.; Sosik, H.M. A submersible imaging-in-flow instrument to analyze nano-and microplankton: Imaging FlowCytobot. *Limnol. Oceanogr. Methods* **2007**, *5*, 195–203. [CrossRef]
23. Ozcan, A.; McLeod, E. Lensless imaging and sensing. *Annu. Rev. Biomed. Eng.* **2016**, *18*, 77–102. [CrossRef]
24. Roy, M.; Seo, D.; Oh, S.; Yang, J.W.; Seo, S. A review of recent progress in lens-free imaging and sensing. *Biosens. Bioelectron.* **2017**, *88*, 130–143. [CrossRef] [PubMed]
25. Seo, S.; Su, T.W.; Tseng, D.K.; Erlinger, A.; Ozcan, A. Lensfree holographic imaging for on-chip cytometry and diagnostics. *Lab Chip* **2009**, *9*, 777–787. [CrossRef] [PubMed]
26. Mudanyali, O.; Bishara, W.; Ozcan, A. Lensfree super-resolution holographic microscopy using wetting films on a chip. *Opt. Express* **2011**, *19*, 17378–17389. [CrossRef] [PubMed]
27. Merola, F.; Memmolo, P.; Bianco, V.; Paturzo, M.; Mazzocchi, M.G.; Ferraro, P. Searching and identifying microplastics in marine environment by digital holography. *Eur. Phys. J. Plus* **2018**, *133*, 1–6. [CrossRef]
28. Kun, J.; Smieja, M.; Xiong, B.; Soleymani, L.; Fang, Q. The Use of Motion Analysis as Particle Biomarkers in Lensless Optofluidic Projection Imaging for Point of Care Urine Analysis. *Sci. Rep.* **2019**, *9*, 17255. [CrossRef]
29. Mahoney, E.; Kun, J.; Smieja, M.; Fang, Q. Point-of-care urinalysis with emerging sensing and imaging technologies. *J. Electrochem. Soc.* **2019**, *167*, 037518. [CrossRef]
30. Lu, C.H.; Shih, T.S.; Shih, P.C.; Pendharkar, G.P.; Liu, C.E. Finger-powered agglutination lab chip with CMOS image sensing for rapid point-of-care diagnosis applications. *Lab Chip* **2020**, *20*, 424–433. [CrossRef]
31. Göröcs, Z.; Tamamitsu, M.; Bianco, V.; Wolf, P.; Roy, S.; Shindo, K.; Yanny, K.; Wu, Y.; Koydemir, H.C.; Rivenson, Y.; et al. A deep learning-enabled portable imaging flow cytometer for cost-effective, high-throughput, and label-free analysis of natural water samples. *Light Sci. Appl.* **2018**, *7*, 66. [CrossRef]

32. Boddy, L.; Morris, C.W.; Wilkins, M.F.; Al-Haddad, L.; Tarran, G.A.; Jonker, R.R.; Burkill, P.H. Identification of 72 phytoplankton species by radial basis function neural network analysis of flow cytometric data. *Mar. Ecol. Prog. Ser.* **2000**, *195*, 47–59. [CrossRef]

33. Coskun, A.F.; Su, T.W.; Ozcan, A. Wide field-of-view lens-free fluorescent imaging on a chip. *Lab Chip* **2010**, *10*, 824–827. [CrossRef] [PubMed]

34. Shanmugam, A.; Salthouse, C. Lensless fluorescence imaging with height calculation. *J. Biomed. Opt.* **2014**, *19*, 016002. [CrossRef] [PubMed]

35. Paiè, P.; Vázquez, R.M.; Osellame, R.; Bragheri, F.; Bassi, A. Microfluidic Based Optical Microscopes on Chip. *Cytom. Part A* **2018**, *93*, 987–996. [CrossRef] [PubMed]

36. Pang, S.; Han, C.; Lee, L.M.; Yang, C. Fluorescence microscopy imaging with a Fresnel zone plate array based optofluidic microscope. *Lab Chip* **2011**, *11*, 3698–3702. [CrossRef]

37. Sommer, U.; Charalampous, E.; Genitsaris, S.; Moustaka-Gouni, M. Benefits, costs and taxonomic distribution of marine phytoplankton body size. *J. Plankton Res.* **2017**, *39*, 494–508. [CrossRef]

38. Borowitzka, M. *Microalgae in Health and Disease Prevention*; Academic Press: Cambridge, MA, USA, 2018.

39. Salomé, P.A.; Merchant, S.S. A Series of Fortunate Events: Introducing Chlamydomonas as a Reference Organism. *Plant Cell* **2019**, *31*, 1682–1707. [CrossRef]

40. Toyama, T.; Kasuya, M.; Hanaoka, T.; Kobayashi, N.; Tanaka, Y. Growth promotion of three microalgae, *Chlamydomonas reinhardtii*, *Chlorella vulgaris* and *Euglena gracilis*, by in situ indigenous bacteria in wastewater effluent. *Biotechnol. Biofuels* **2018**, *11*, 176. [CrossRef]

41. McCree, K.J. The action spectrum, absorptance and quantum yield of photosynthesis in crop plants. *Agric. Meteorol.* **1972**, *9*, 191–216. [CrossRef]

42. Dadi, H.S.; Pillutla, G.K.M. Improved face recognition rate using HOG features and SVM classifier. *IOSR J. Electron. Commun. Eng.* **2016**, *11*, 34–44. [CrossRef]

43. Kristan, M.; Leonardis, A.; Matas, J.; Felsberg, M.; Pflugfelder, M.; Cehovin Zajc, L.; Vojir, T.; Bhat, G.; Lukezic, A.; Eldesokey, A.; et al. The sixth visual object tracking vot2018 challenge results. In Proceedings of the European Conference on Computer Vision, Munich, Germany, 8–14 September 2018.

44. Latychevskaia, T.; Fink, H. Practical algorithms for simulation and reconstruction of digital in-line holograms. *Appl. Opt.* **2015**, *54*, 2424–2434. [CrossRef]

45. Ector, L. *River Algae*; Springer International Publishing: Cham, Switzerland, 2016.

46. Xiong, B.; Fang, Q. Luminescence lifetime imaging using a cellphone camera with an electronic rolling shutter. *Opt. Lett.* **2020**, *45*, 81–84. [CrossRef]

47. Geelen, B.; Tack, N.; Lambrechts, A. A compact snapshot multispectral imager with a monolithically integrated per-pixel filter mosaic. In Proceedings of the Advanced Fabrication Technologies for Micro/Nano Optics and Photonics VII, San Francisco, CA, USA, 7 March 2014; Volume 8974.

48. Zhang, Y.; Xu, C.-Q.; Guo, T.; Hong, L. An automated bacterial concentration and recovery system for pre-enrichment required in rapid *Escherichia coli* detection. *Sci. Rep.* **2018**, *8*, 17808. [CrossRef] [PubMed]